

Faculty of Bioscience Engineering

LBRES2101 - SMART TECHNOLOGIES FOR ENVIRONMENTAL ENGINEERING INTEGRATED PROJECT

Authors: Abdullah Toqeer, Catherine Akinyi Odera, Lilian Akudo Akanazu, Sourav
Kamakar, Maxime Mulamba Ke Tchomba

Lecturer(s): Francois Jonard, Sebastien Lambot

Assistant(s): Maxime Thomas, Maud Henrion

Academic year: 2022-2023
Bioscience Engineering

Table of Contents

Table of Figures.....	3
Table of Tables	3
List of Acronyms	4
1. Introduction	5
1.1. Objectives.....	5
1.2. Study Area.....	5
2. Materials and methods.....	6
2.1. GPR.....	6
2.1.1. Data collection:	6
2.1.2 Data processing.....	8
2.2.EMI	8
2.2.1 Data collection:	8
2.2.2 Data processing:.....	9
2.3. Photogrammetry	9
3. Results.....	10
3.1 GPR.....	10
3.2. EMI	16
3.3. Photogrammetry	20
4. Discussion	22
5. Conclusion	25
6. Bibliographic references	26
7. Annexes.....	27

Table of Figures

Figure 1:Study area map	6
Figure 2:Map of GPR transects.....	7
Figure 3:GPR vertical slice from position x=0 to x=0.15m	11
Figure 4:GPR vertical slice from position x=0.15 to x=0.3m	11
Figure 5:GPR vertical slice from position x=0.3 to x=0.45m	12
Figure 6:GPR vertical slice from position x=0.45 to x=0.6m	12
Figure 7:GPR vertical slice from position x=0.6 to x=0.75m	13
Figure 8:GPR vertical slice from position x=0.75 to x=0.9m	13
Figure 9:GPR vertical slice from position x=0.9 to x=1.05m	14
Figure 10:GPR vertical slice from position x=1.05 to x=1.2m	14
Figure 11:GPR vertical slice from position x=1.2 to x=1.35m	15
Figure 12:GPR vertical slice from position x=1.35 to x=1.5 m	15
Figure 13:GPR horizontal slice at z=0.001m.....	16
Figure 14:Conductivity results of the study area and kriging results of the EC of points collected	17
Figure 15:DEM of the study area with simplified contours showing elevation	18
Figure 16:Kriging analysis using the first group's EMI data and Kriging analysis using the third group's EMI data	19
Figure 17:DSM evaluation of Photogrammetry model and ERUISSO1 model against LIDAR .	20
Figure 18:Contour comparison of data from Photogrammetry, ERUISSOL and Relief Wallonia	22
Figure 19:Comparison between EMI results and GPR observation	23
Figure 20:Comparison between EMI and DSM results.....	24

Table of Tables

Table 1: Parameters to generate vertical slices.....	8
Table 2: Root mean-square error (RMSE), mean error (ME) and standard deviation (STD) of DEM with respect to. PICC	21

List of Acronyms

CRS - Coordinate Reference System

DEM - Digital Elevation Model

DSM - Digital Surface Model

EC - Electromagnetic Conductivity

EMI - Electromagnetic Induction

ERRUISSOL - EROsion RUISSellement Sol

GPR - Ground Penetrating Radar

LiDAR - Light Detection and Ranging

PICC – Projet Informatique de Cartographie Continue

SRTM – Shuttle Radar Topography Mission

1. Introduction

Sustainable agriculture has evolved over the years with the introduction of non-invasive technological applications to study the sub-surface characteristics of agricultural land parcels. The role of smart technology in agriculture includes the adoption of various innovations, such as sensor technology, machine learning, positioning systems, etc., to examine the vegetative composition, soil properties, and topography of landscapes. Because of the increased environmental stress, the demand for sustainable agriculture is rising. Consequently, it is important to understand and study the surface and subsurface properties. In the non-destructive testing methods, GPR is widely used to study the subsurface properties of the ground (YJ Teoh et al., 2018; Gish et al., 2002; Lombardi et al., 2022; Yan et al., 2022). Similarly, EMI is also used to study the subsurface properties and complement the results of GPR (Saey et al., 2014; Huang et al., 2015; Martinez et al., 2018; Moghadas et al., 2017). While for surface properties, aerial photogrammetry is used (Walstra et al., 2007; jakopec et al., 2022; Marzolf & Poesen, 2009; Hapke & Richmond, 2000). On this premise, this project is focused on utilizing smart technology applications - EMI, GPR, and Drone technology to study the characteristics of the study area.

1.1. Objectives

The general objective of this project is to carry out site characterization of the study area. Specific objectives include determining;

1. The properties of the soil using EMI (electrical conductivity)
2. The surface properties using photogrammetry (topography and orthophoto)
3. The properties of the subsoil using GPR.

1.2. Study Area

The study area selected for this project was located at 50°40.949 North and 4°37.320 East near the UCLouvain - Ferme de Lauzelle, as shown in Figure 1. There is an artificial lake situated in the northeastern part of the study area. The ground control points shown in the study area map were marked for the orientation in the photogrammetry task. The soil type of the study area is silt, denoted as “Abp” in the Carte Numerique des Sols de Wallone as shown in figure A-5 in annex. The detailed description of Abp according to the legend is attached in figure A-6 and A-7 in the Annex and is explained as follows:

- A = Texture (FR: Limon, ENG: Silt)
- b = Drainage (FR : favorable-non gleyifiés, ENG: favorable-ungleyed)
- p = Profile Development (FR: Absence de développement de profil, ENG: Absence of profile development)



Figure 1: Study area map

2. Materials and methods

2.1. GPR

2.1.1. Data collection:

The study area was covered in 10 lines, out of which nine were parallel to each other. Ideally, all the lines should be close to each other and of equal length to do the horizontal interpolation. In our data acquisition, only lines (8,9) and (7,10) were of equal length.

Consequently, this made data processing and interpretation difficult as the interpolation was not done correctly. The data acquisition map of the study area is shown in Figure 2.



Figure 2: Map of GPR transects

a) GPR Setting

In the computer setting, the main step is creating the project file, followed by the selection of the survey wheel for positioning. The “Utility (for utility detection)” was chosen for the configuration type setting, and a 400MHz antenna was selected, which is installed on the device. 100 scans/meter was chosen for the number of scans, corresponding to one measurement per centimetre.

For the shift in signal setting, the time range was selected from 0 - 50 ns. The Auto gain function setting was changed to a manual function and adjusted to almost $\frac{2}{3}$ of the saturation of the largest reflection. The centre frequency was set to 400MHz, i.e., the frequency of the antenna installed on the device. The lower useful frequency was set to 100 MHz, i.e., the centre frequency divided by 4. Finally, the low pass frequency was set to approximately 900 MHz, i.e., a bit more than twice the centre frequency.

2.1.2 Data processing

i. Generating the vertical and horizontal slices

The code used to process the GPR data and generate the horizontal and vertical slices was obtained from the lab session exercise. No changes were made to generate the horizontal slices. However, the following changes as shown in table 1 were made to the code according to the data processing requirements for the vertical ones.

Table 1: Parameters to generate vertical slices

Parameter	Value
Number of images	10
Time range	0 - 50e-9 ns
Antenna's frequency range	100e6 - 900e6
Average profile length	100m
Depth correction	0.4
Gain function	3
Dielectric constant	16 (As the material in the study area was mainly silty according to soil map). (Timo Saarenketo, 2006).

The complete modified code is provided along with the report.

2.2.EMI

2.2.1 Data collection:

The EM38 electromagnetic meter attached to the bottom of a motor truck was used to measure the conductivity of the soil in the study area. The first group carried out the calibration exercise, and we confirmed that the calibration satisfied the parameters for the measurement before starting data collection. We checked the instrument's sound by driving the truck a few meters to our starting point in the study area. Then, the truck was driven around the study area while ensuring no interference of any external metal instrument that

may interfere with the data. A computer attached to the device documented the collected data in several files (alt, lat, lon, pos, sigma, and strem38) where the sigma file contains the soil conductivity with their geolocation.

2.2.2 Data processing:

The collected dataset was processed using Microsoft excel. Major pre-processing steps includes converting coordinates to decimal degrees, unit conversion from Siemens to milli-Siemens per second (mS/s), and merging and filtering outliers. The cleaned dataset was then imported into the ArcGIS environment and reprojected to Belgian National CRS (Lambert Belge 1972) for spatial interpolation. We used simple Kriging prediction of our measured conductivity points to interpolate conductivity and make a continuous map over the study area. The kernel function was set at exponential to have an infinite series of multiplication and addition of the kernel to make it valid and estimate random variables for missing points.

For normal score transformation of the data, as shown in Figure A1 in the annexes, the approximation method was set as multiplicative skewing. The semi-variogram in the annex (Figure A2) was left at the default covariance function to calculate the squared difference between the values of the known points around the unknown points, and estimate the dependent values that depend on the model for autocorrelation. To search for neighbourhood points, we set the maximum number of neighbours at 5 and the minimum at 2 so that our assumed locations will not be too far from the prediction locations so as not to have fewer auto-correlated values. The cross-validation method used (annex Figure A4) was the 'leave-one-out' method, where the model leaves a point out and uses the other points to predict the location of the removed point. The result of the cross-validation process of the model confirms that the model almost accurately predicts the interpolated values. The standardized root-mean-square error was 0.91 (91%), close to 1, showing an accurate variability prediction.

2.3. Photogrammetry

This method consists of obtaining reliable information about the surface of the study area based on images. A Phantom 4 Pro drone flew over the area to collect 60 camera pictures of 3000 by 4000 pixels.

The first step towards computing a Digital Elevation Model (DEM) is to load images into Agisoft Metashape and align cameras, as each photo was embedded with GPS coordinates. The software generates 100000 tie points from which it computes dense cloud points. To improve the accuracy of the projection, each image was manually annotated with the locations of Ground Control Points, whose coordinates were provided (see Figure 1). Note that point 1 was discarded due to difficulty locating it in images. Differential GPS enables centimetre precision, which allows a high resolution. The resulting DSM and Orthophoto were rendered at 0.05m per pixel resolution.

3. Results

3.1 GPR

a) Horizontal Slices

A total of 10 vertical slices were generated from the GPR radargrams obtained from the field using the Matlab software. The slices range from 0 to 1.5 meters as represented in Figures (3-12), alongside images of their frequency profiles. From the slices, we can interpret the characteristics of the subsurface soil layers within the area surveyed. Generally, the soil properties are slightly changing, as shown by the variation in the value of reflectance in the slices as one moves from figure 3 to Figure 12.

The slices in Figures 3,4,5,8,9 and 12, outlined by the yellow bounding box, show the presence of change in the soil property indicated by the high reflection around that zone compared to the neighbouring layers, this may be due to the presence of soil horizon or a rock. In addition, the vertical slices (Figures 4,6,7,10,11 and 12), marked by orange lines and the yellow bounding boxes, exhibit high amplitude reflections. High amplitude may be probably because of the presence of transitional zones of soils with different properties or a water table probably because these transects were located around the water body.

Figures 7 and 11 show that the regions marked by orange lines have high electric conductivity and magnetic permeability, characterized by high attenuation resulting in shallow subsurface imaging. Figure 6 shows a point within the slice with a reflection hyperbola that may result from an object beneath the ground. The object is possibly a pipe since this slice corresponds to transect line 4 (see Figure 2), which was taken over a region with an underground pipe. In Figure 9 corresponding to transect 7, apart from the region in

the yellow bounding box which may result from a soil transition zone, the rest of the soil within the transect seems to be homogeneous evident by the presence of low amplitude values.

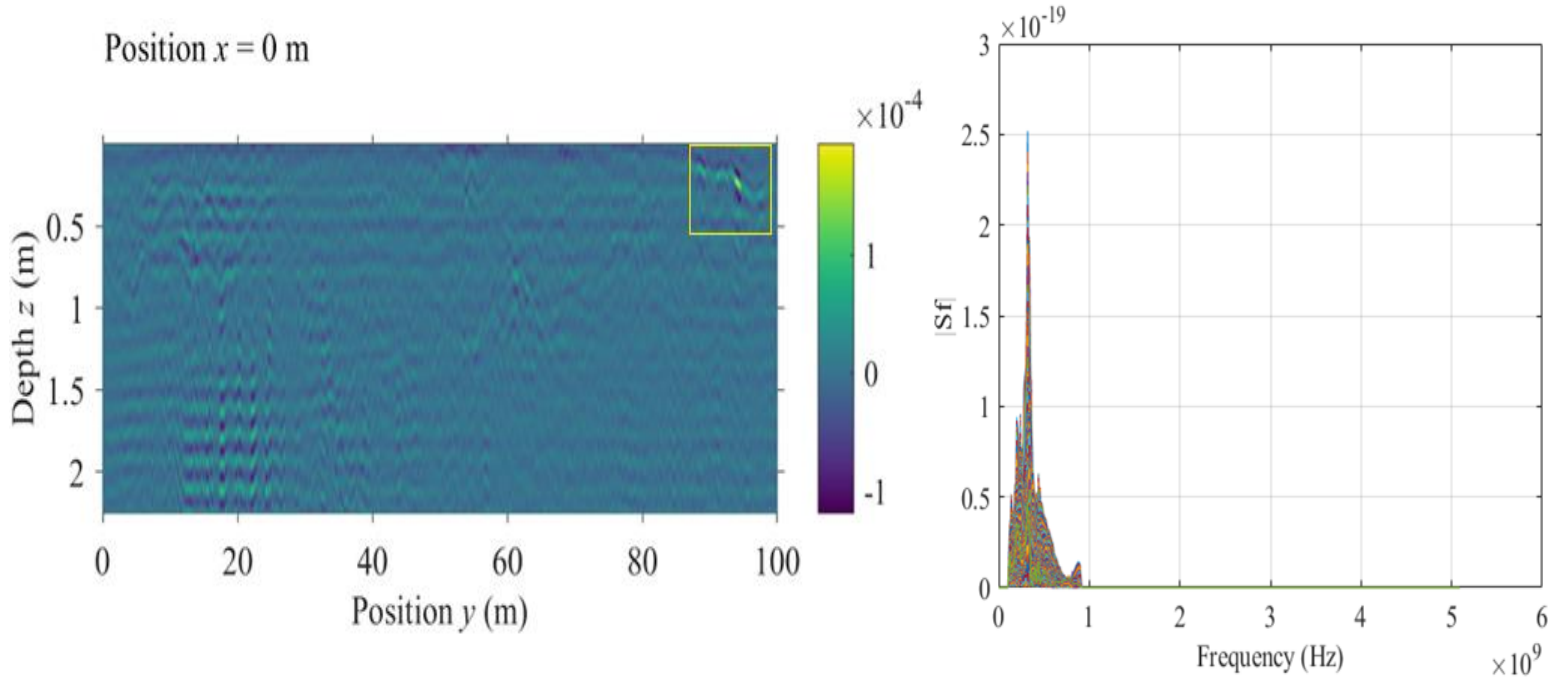


Figure 3:GPR vertical slice from position $x=0$ to $x=0.15\text{m}$

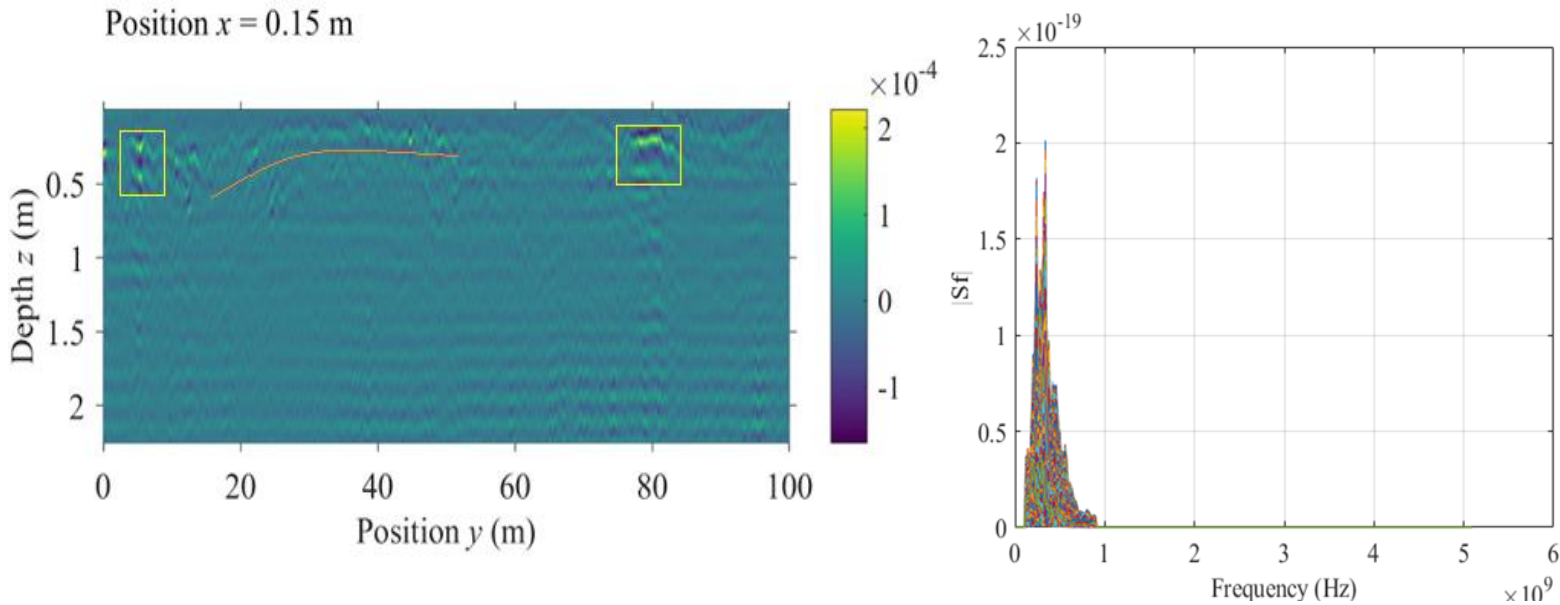


Figure 4:GPR vertical slice from position $x=0.15$ to $x=0.3\text{m}$

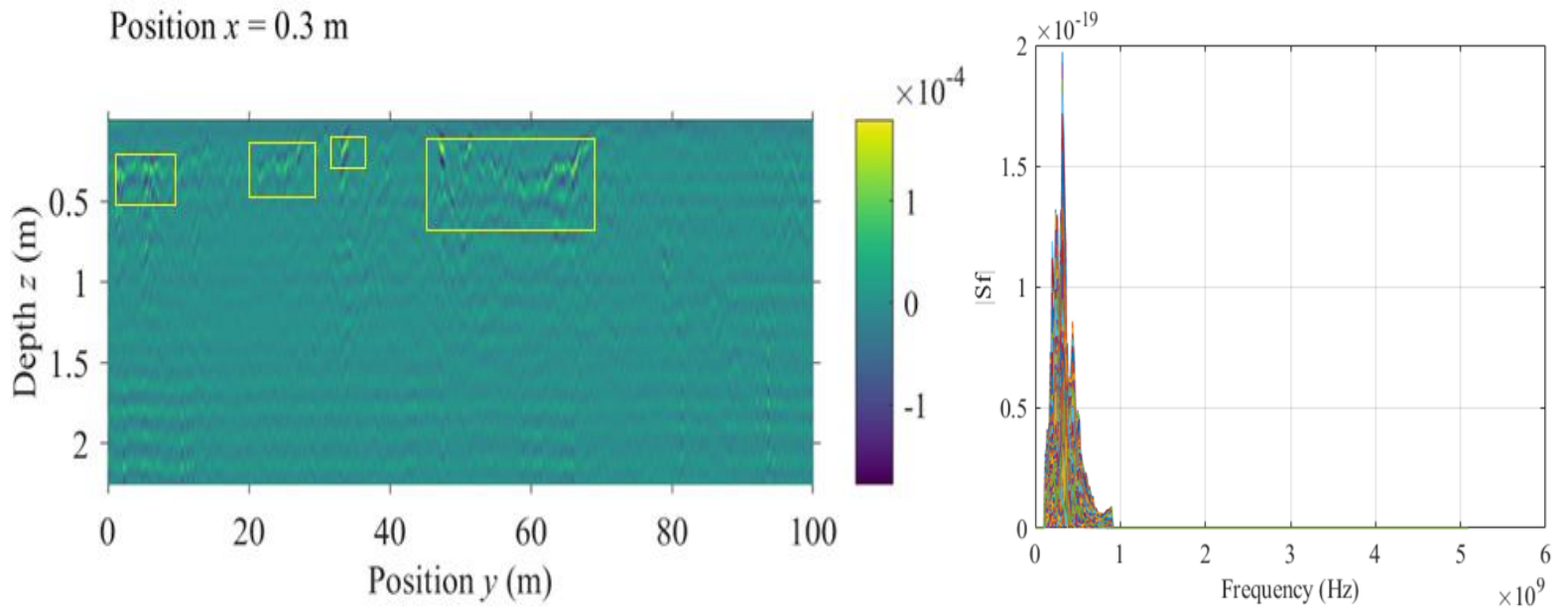


Figure 5:GPR vertical slice from position $x=0.3$ to $x=0.45$ m

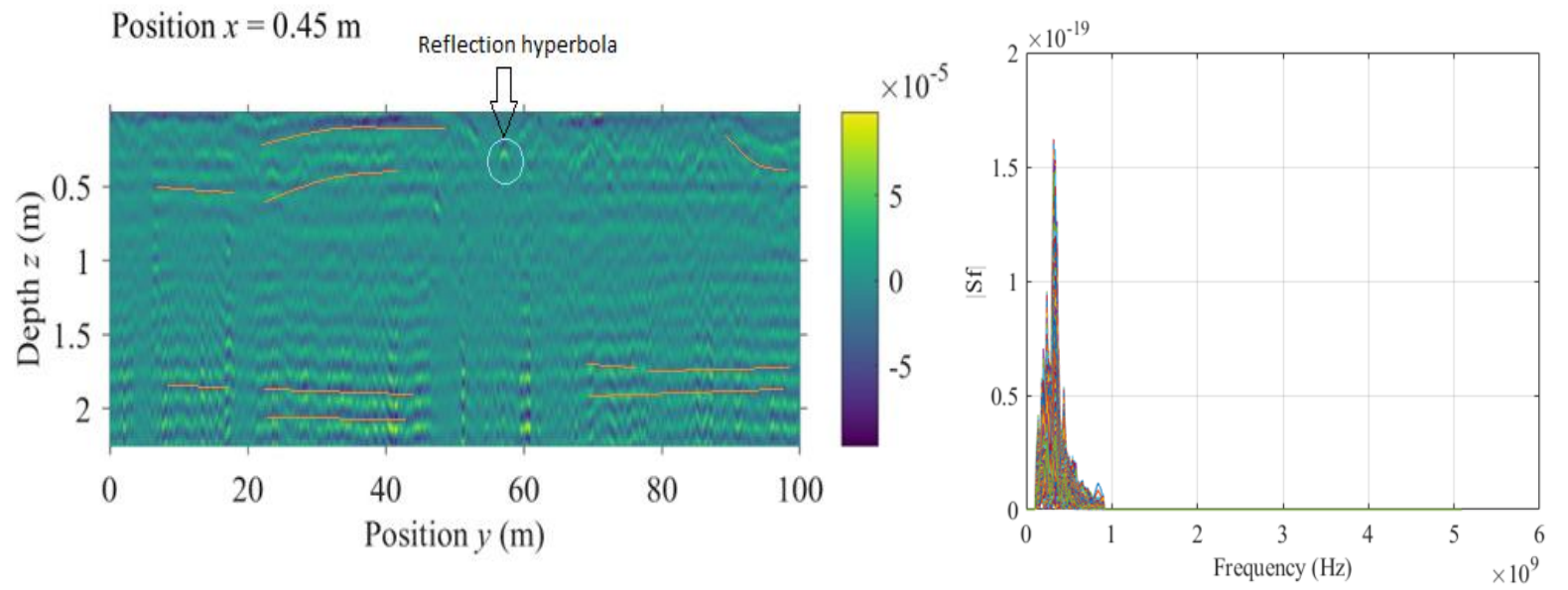


Figure 6:GPR vertical slice from position $x=0.45$ to $x=0.6$ m

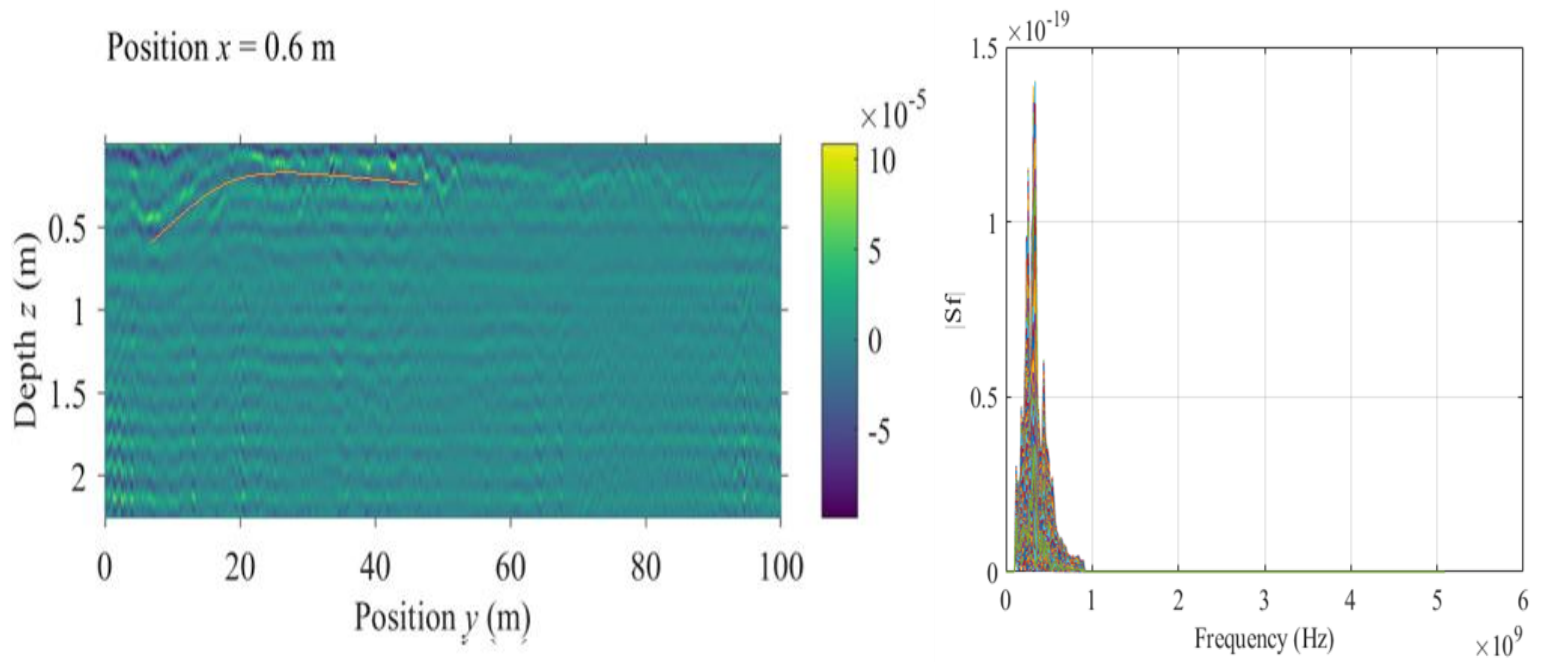


Figure 7: GPR vertical slice from position $x=0.6$ to $x=0.75$ m

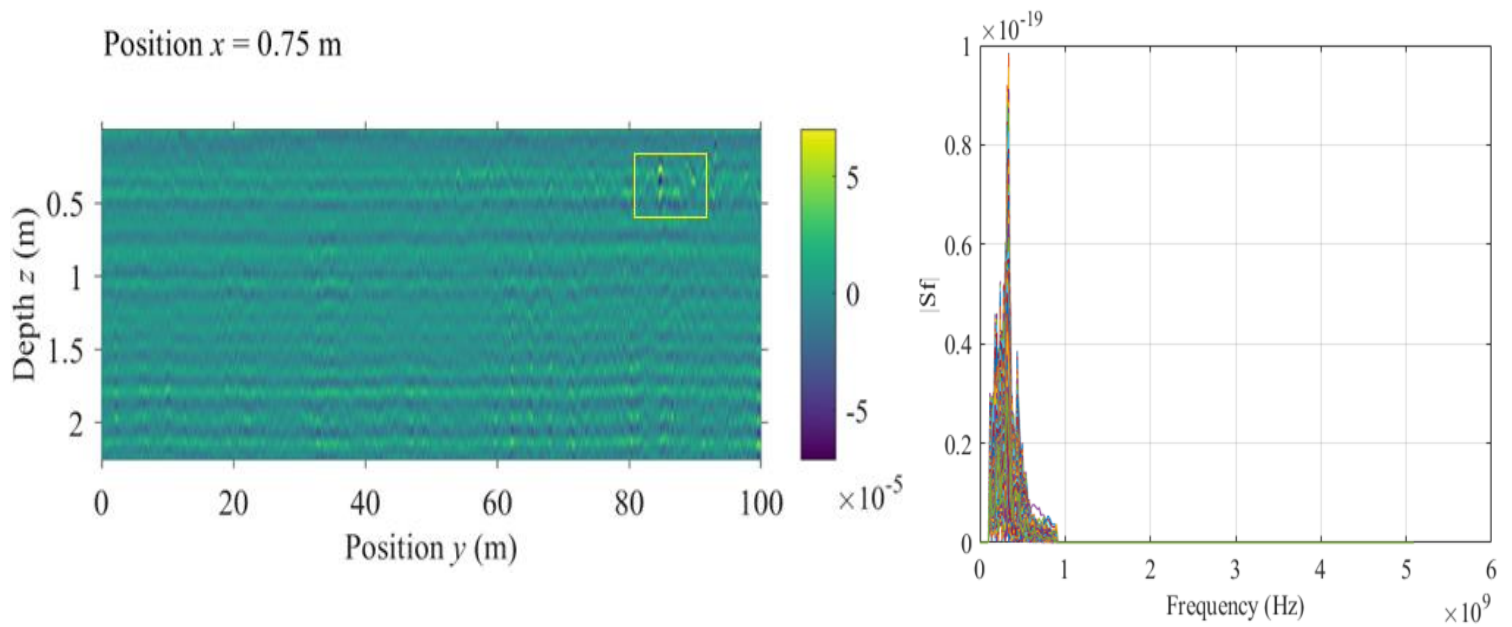


Figure 8: GPR vertical slice from position $x=0.75$ to $x=0.9$ m

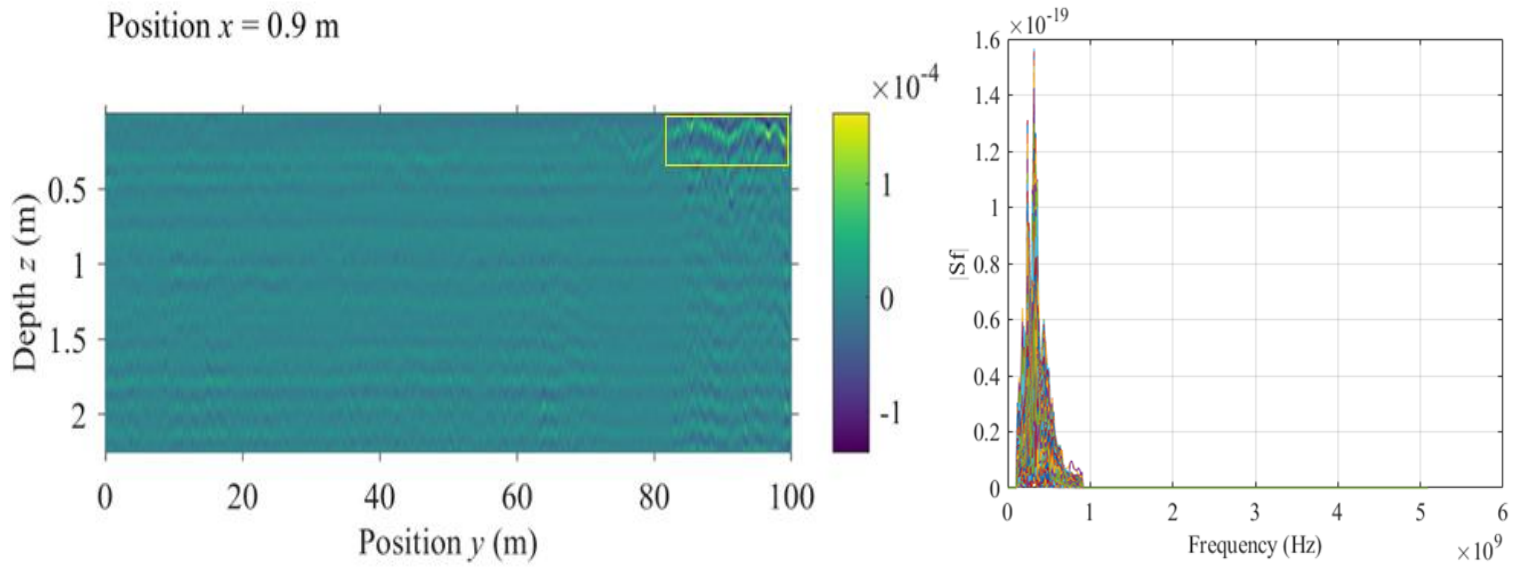


Figure 9:GPR vertical slice from position $x=0.9$ to $x=1.05$ m

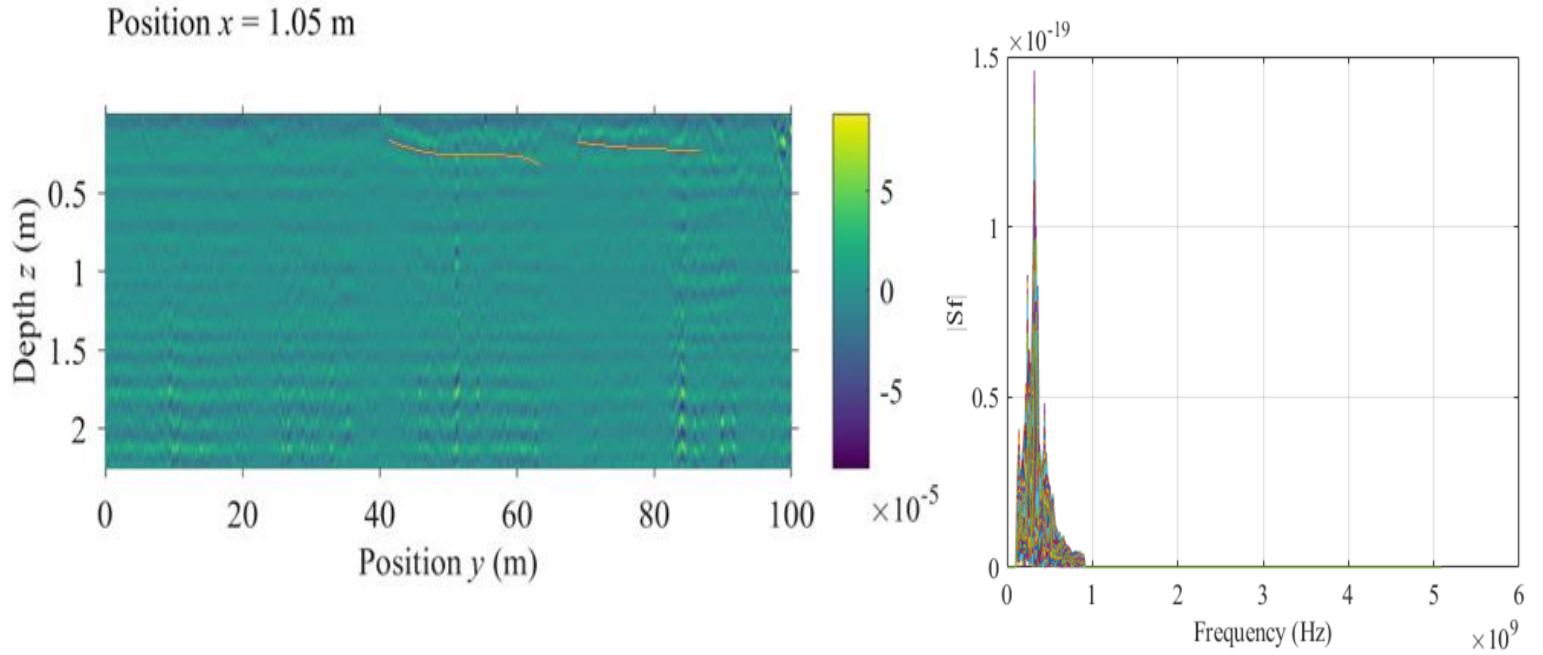


Figure 10:GPR vertical slice from position $x=1.05$ to $x=1.2$ m

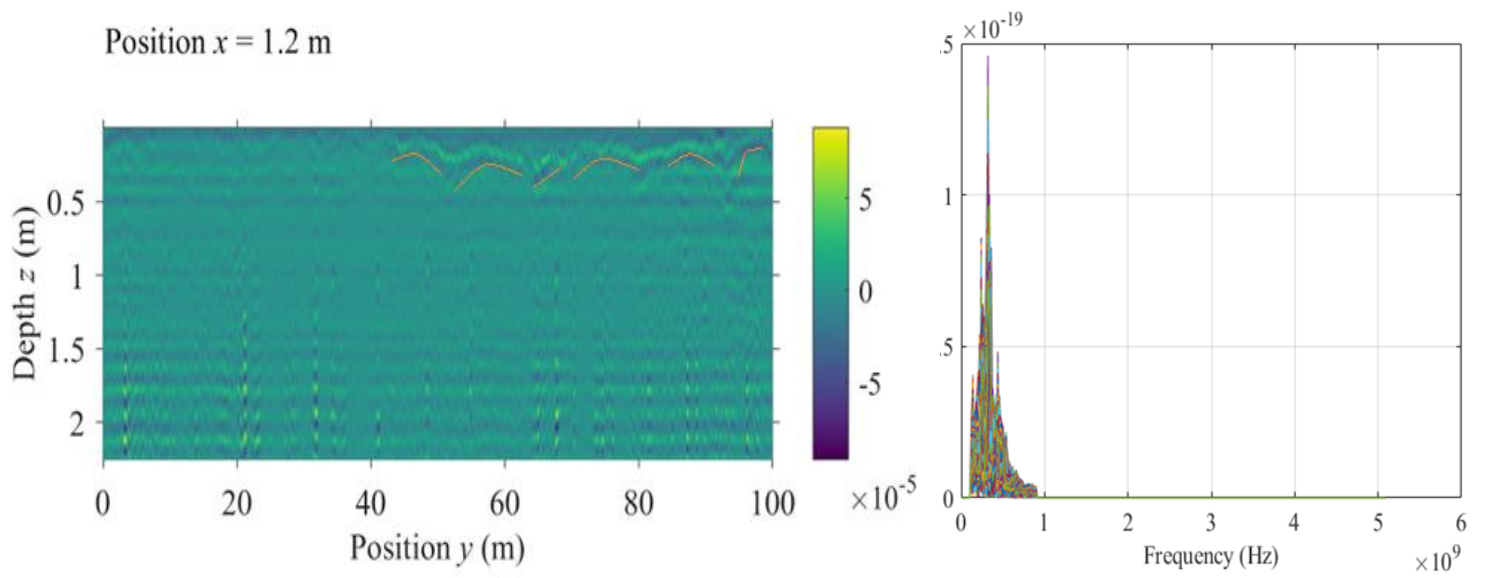


Figure 11: GPR vertical slice from position $x=1.2$ to $x=1.35$ m

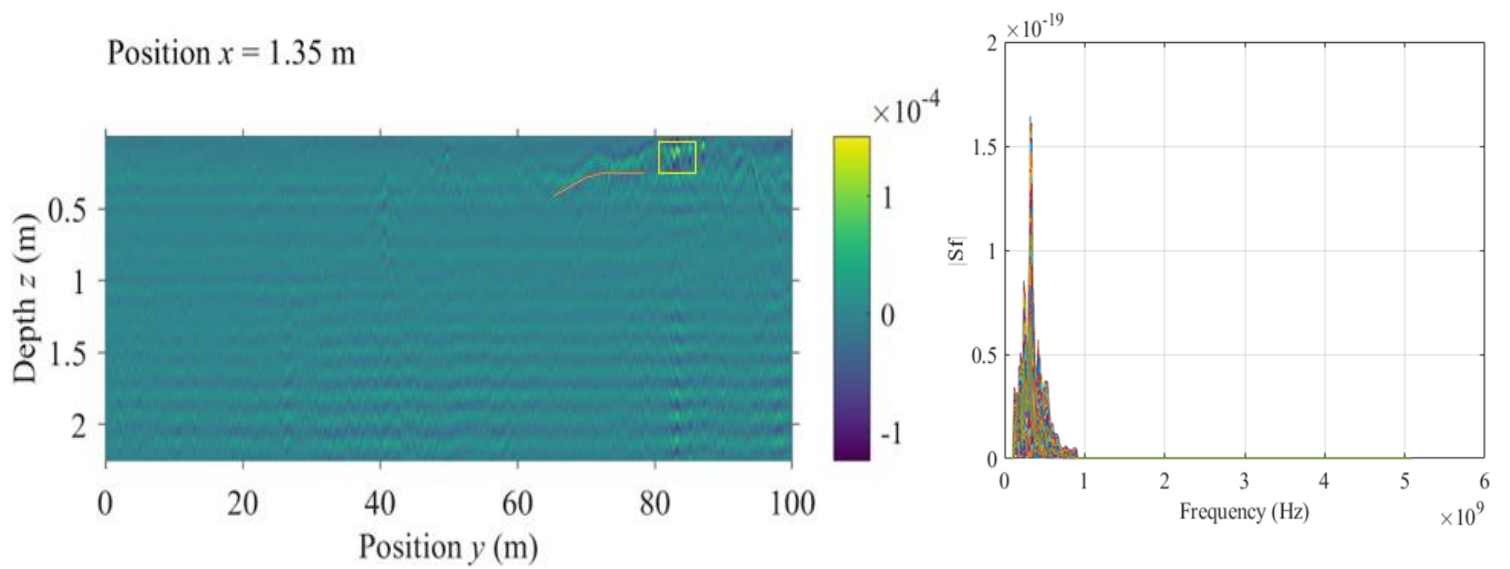


Figure 12: GPR vertical slice from position $x=1.35$ to $x=1.5$ m

b) Horizontal Slices

Eight hundred and ninety horizontal slices were generated from the GPR radargrams produced in the field. As discussed in the GPR data collection section, all the lines were not closed and of equal length, which caused difficulty in data processing and interpretation. An example of a horizontal slice generated from the radargram is shown in Figure 13. However, due to poor interpolation caused by the lack of transects that were close together and of the same size, no useful information could be deduced from the horizontal slices. The processed horizontal slices are included together with the report.

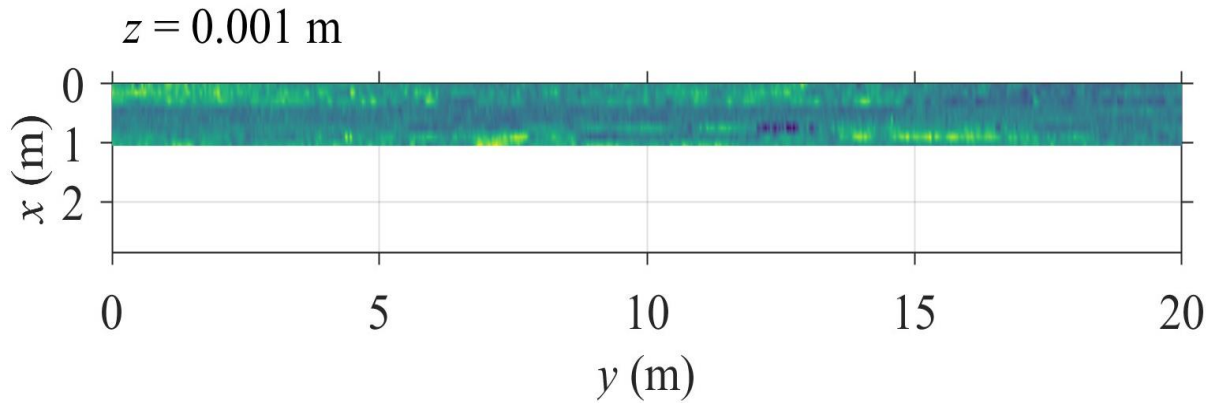


Figure 13:GPR horizontal slice at $z=0.001\text{m}$

3.2. EMI

In Figure 1 above, the study area map shows the points of sampling, the ground control points and the border of the area of interest. The area of interest used in this analysis was smaller than the study area map shared because we do not want the interpolated areas to be farther away from the source points, as this would affect the accuracy of the prediction model.



Figure 14: Conductivity results of the study area and kriging results of the EC of points collected

The map in Figure 14(A) above shows the soil conductivity at different points in the study area. It is observed that points along the closest buffer to the lake recorded lower conductivity, but the points recorded on the northern and southern parts of the lake have higher conductivity. On the other hand, areas under the canopy at the east and west of the field have higher conductivity. The results of the kriging (Figure 14(B)) shows that the northern part of the lake (a slopy area near the lake) have higher conductivity which is because of soil water movement towards the lake, converging with the field observation. Also, the vegetative buffer showed higher conductivity in the eastern and northern parts representing the field situation.

The waterbody and areas around it showed the least conductivity because of interpolating lower values near the lake, which is unrealistic. Ideally, a water body should have the highest conductivity value. Also, areas surrounding the field with higher elevation showed higher electromagnetic conductivity, which is not logical since they have lesser water content. Ideally, drier soils have lower conductivity than wetter soils because water contains ions that can propagate electrical currents. However, this was not the same in the

study area, as we noticed that the wetter areas had less conductivity than the drier areas. A factor that could also affect the soil's conductivity is the landscape's porosity, allowing for more water into the soil. Soils with metallic compounds and cation exchange capacity have more electrical conductivity potential than soils without these minerals. To confirm this difference between what is expected and what was observed, we compared this result with the DEM, the EMI data obtained by other groups and the soil map of the area in Figures 15, 16 and A5 below.

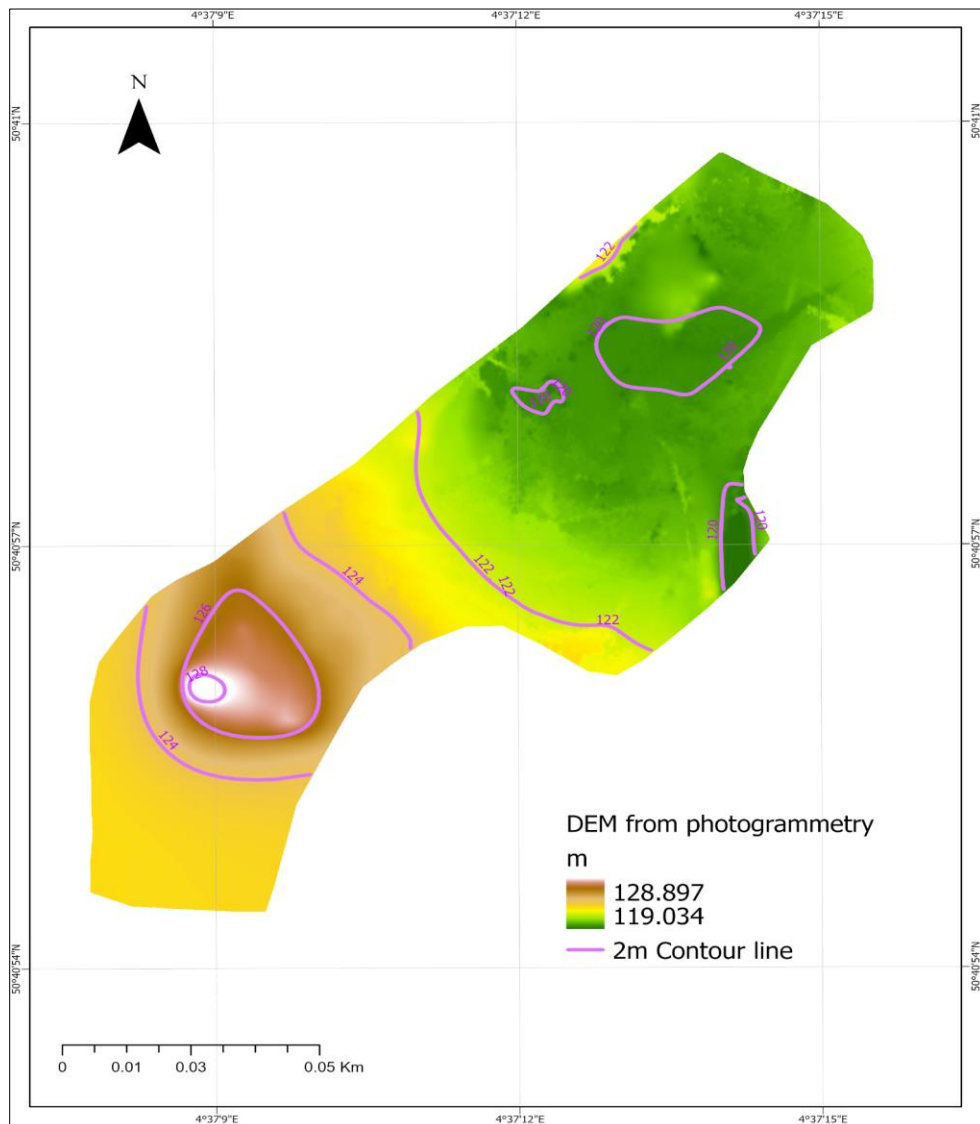


Figure 15:DEM of the study area with simplified contours showing elevation

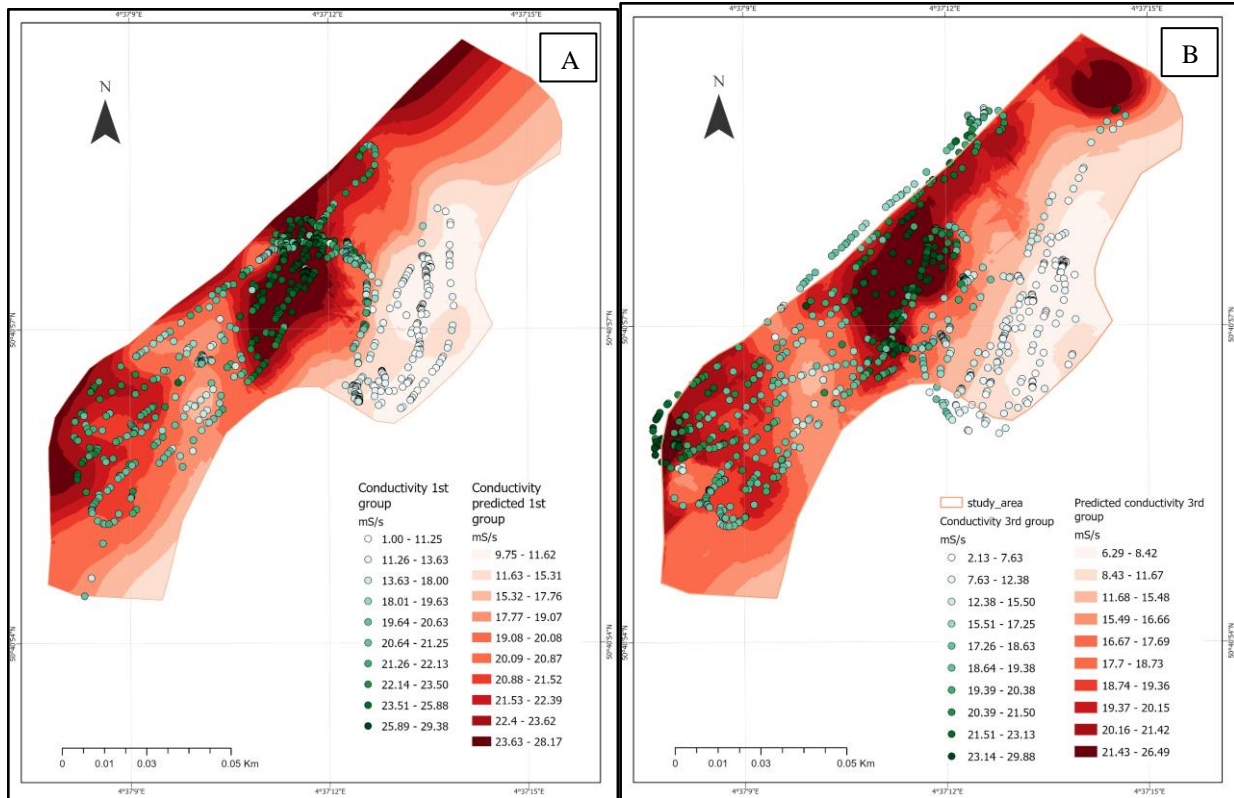


Figure 16:Kriging analysis using the first group's EMI data and Kriging analysis using the third group's EMI data

Comparing the EMI (Figure 14 b) with DEM imagery (Figure 15), we only observed lower conductivity near the highest elevation at the southwestern part. The southern border of the field where we observed high electrical conductivity, has a higher elevation than the northern part of the field towards the lake. Elevation generally affects soil bulk density, which can also increase the EC of the soil with increased height in a given area. This could be a possible explanation for the observed higher conductivity in the soils farther away from the water body because of their elevation. But, in comparison with the dataset of other groups (Figure 16A and 16B), it was observed that these high areas northwards reflected medium conductivity from the EC maps shown from the results. In contrast, the lowlands around the east of the lake reflected the highest conductivity, with few high conductivity points in the far north.

Generally, for both results (first and third groups), the western part of the study area showed higher conductivity than the eastern part, but from our results, both sides of the study area had high conductivity showing more wetness as they are under the canopy. Another

important observation we must note is that these two groups collected fewer points around the lake during their field measurement thus, the kriging analysis interpolated the conductivity collected from the closest points, which were high, resulting in higher conductivity results in those areas. The accuracy in estimating the soil condition for a kriging result depends on the number of points used for the prediction model and how these points are dispersed over space. Although the results of the compared group showed that the field had more conductivity around the water body, which is logical because of the conductivity properties of water and wet soils, it is not safe to use these results as a basis for interpreting the soil condition of the field.

As earlier stated, the dominant soil type in the study area is silt which contains about 5-15% clay particles. Generally, it reflects medium EC values because of its water retention capacity compared to sand (Othaman, *et. al.*, 2020). Also, the soil EC values reflect not just the moisture but also the salinity of the soil. Since the artificial lake in the field is fresh water, it is very likely that the areas around the lake have lower EC values compared to the periphery, because the soil is more saline in those areas.

3.3. Photogrammetry

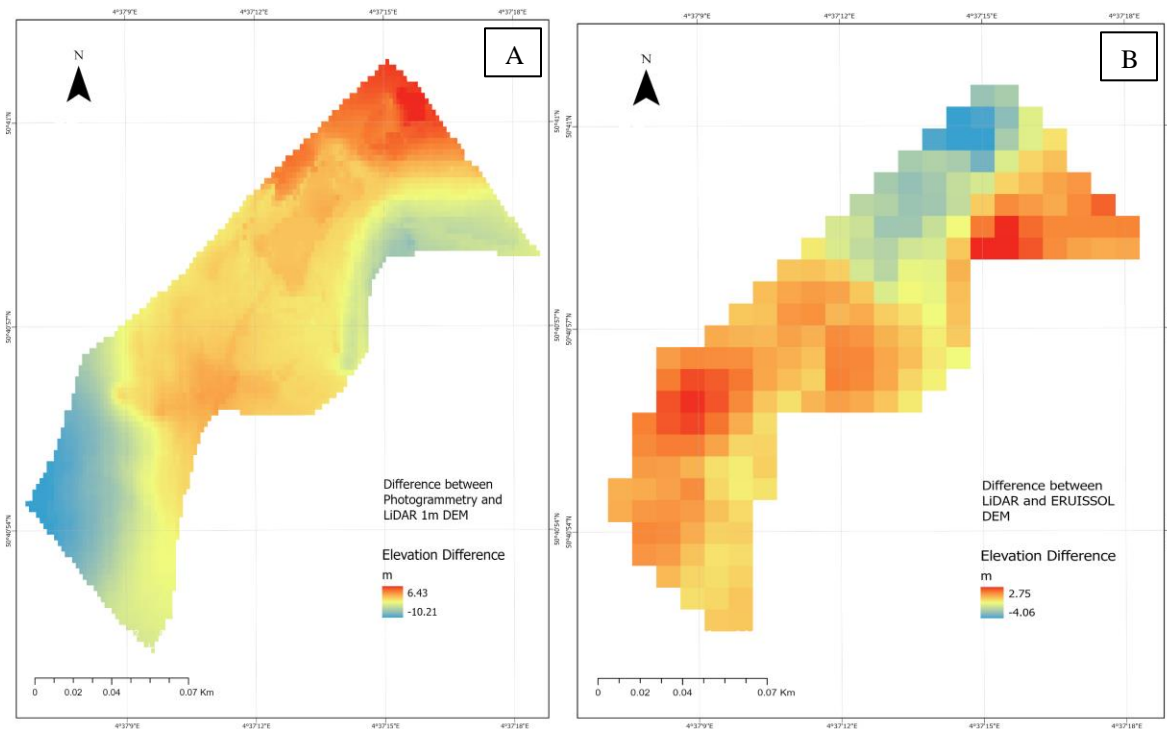


Figure 17:DSM evaluation of Photogrammetry model and ERUISSO1 model against LIDAR

In assessing the quality of the DEM, a proper comparison with ground truth data was required. PICC data contains altitude for selected points obtained by photogrammetry with differential GPS coordinates. Following current practices (Li, Xinchuan, et al. 2017), we evaluate each DEM by sampling and comparing their reported altitude at those points.

Table 2: Root-mean-square error (RMSE), mean error (ME) and standard deviation (STD) of DEM with respect to PICC

	Resolution (m)	RMSE	ME	STD
SRTM	~30	7.424239	6.113334	4.614735
ERRUISSOL	10	1.930573	0.711983	1.965765
PHOTOGRAM	~0.05	1.880030	0.192495	2.048646
LIDAR	1	0.433285	0.198891	0.421680
RELIEF WAL (DSM)	1	0.433285	0.198891	0.421680

As displayed in Table 2, the resolution directly impacts the amplitude of errors, as the photogrammetry DEM achieves the lowest ME. Although not on par with the LIDAR DEM and DSM, the model still achieves a low variance. As expected, most of the discrepancies happened around Ground Control Point 1 (which was discarded), as illustrated in Figure 17 and Figure A8. Photogrammetry and differential GPS provide a low-enough resolution to precisely represent the slope throughout the study area, including the water body. As an example, elevation contours for provided DEM in Figure 18 fail to capture nuances in the water body.

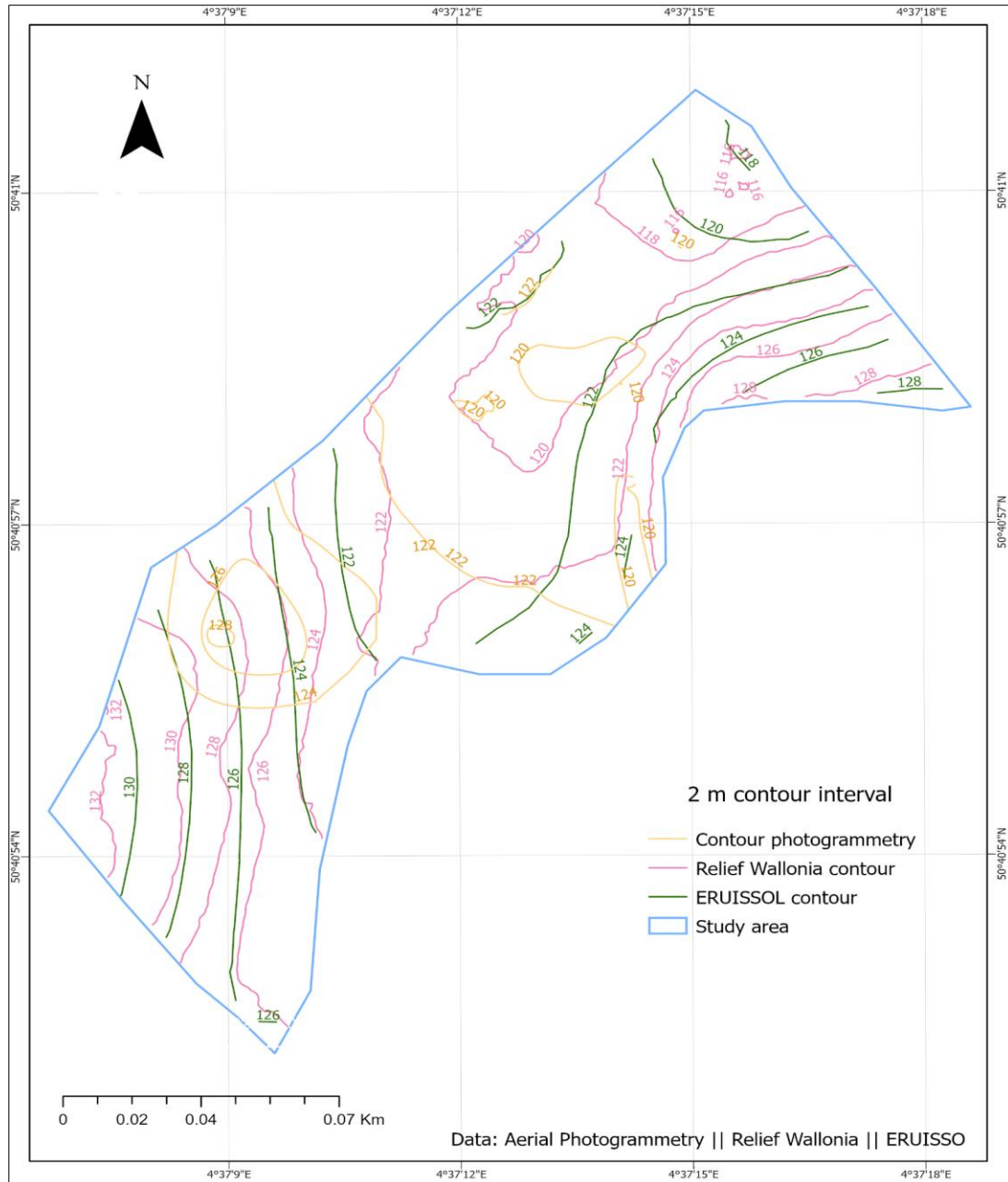


Figure 18: Contour comparison of data from Photogrammetry, ERUISSOL and Relief Wallonia

4. Discussion

The results of the EMI and the GPR were compared to examine the relationship between the soil components, the dielectric constants, and the electromagnetic conductivity of the soil particles. From the GPR results, we observed very interesting wave reflections in transects 7, 3, 5, and 9, as shown in the corresponding Figures 9, 5, 7 and 11 above. The

figure below shows the location of the GPR lines where these transects were generated, overlaying the EC of the field.

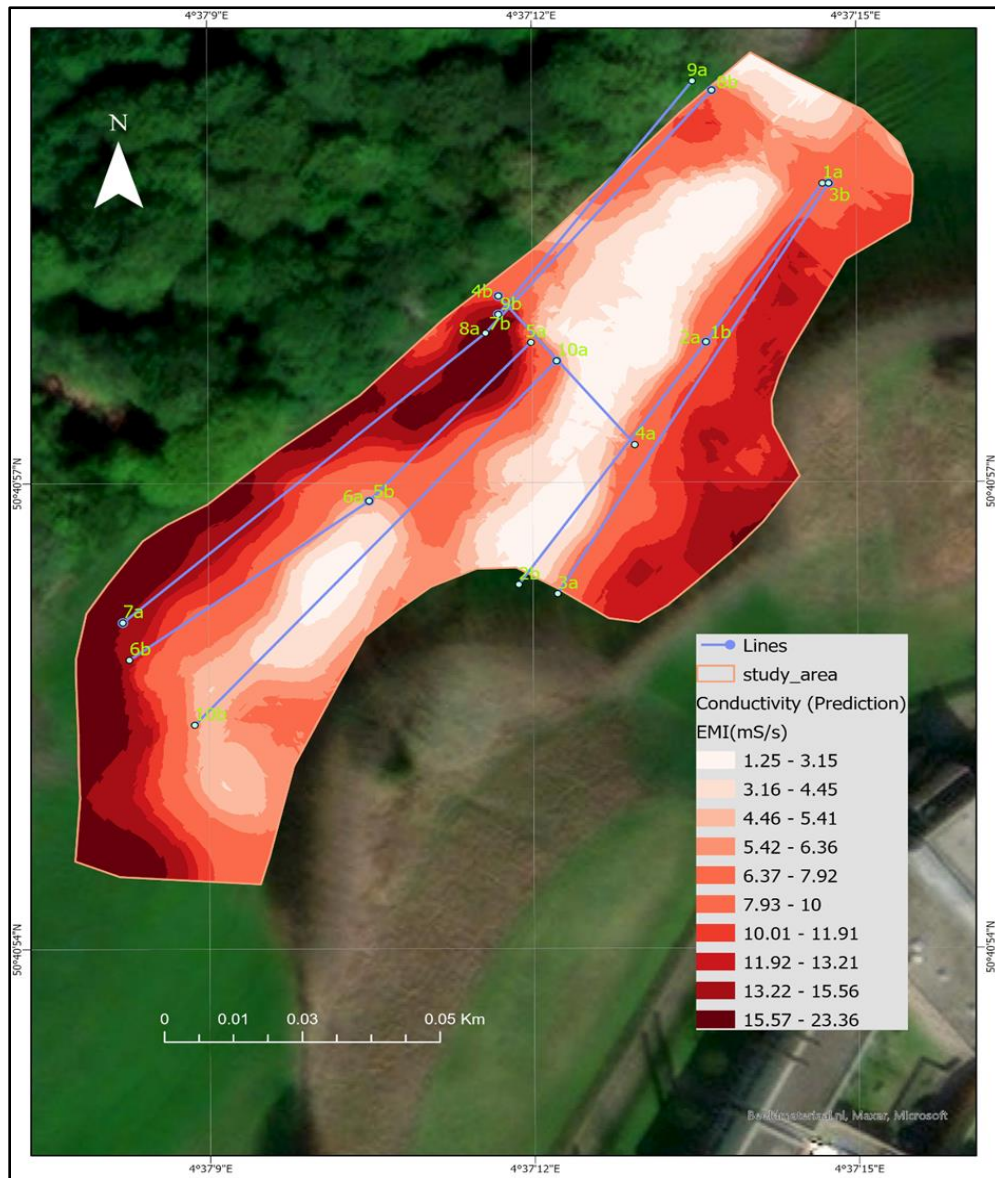


Figure 19: Comparison between EMI results and GPR observation

A pattern was observed between the results of the GPR and the EC conductivity of the soil such that areas where higher wave reflectance was observed also showed high electromagnetic conductivity. For example, the soil conductivity in line 7 above shows a homogenous soil at the beginning (7a) with an increased reflectance towards the end (7b), which corresponds to the results of the generated EC. Also, in lines 5a and 9b, high conductivity was observed, corresponding to the high conductivity values from the kriging results observed in these areas.

The results of the EMI and DSM analyses were also compared to examine the relationship between the canopy height and the EC of the soil.

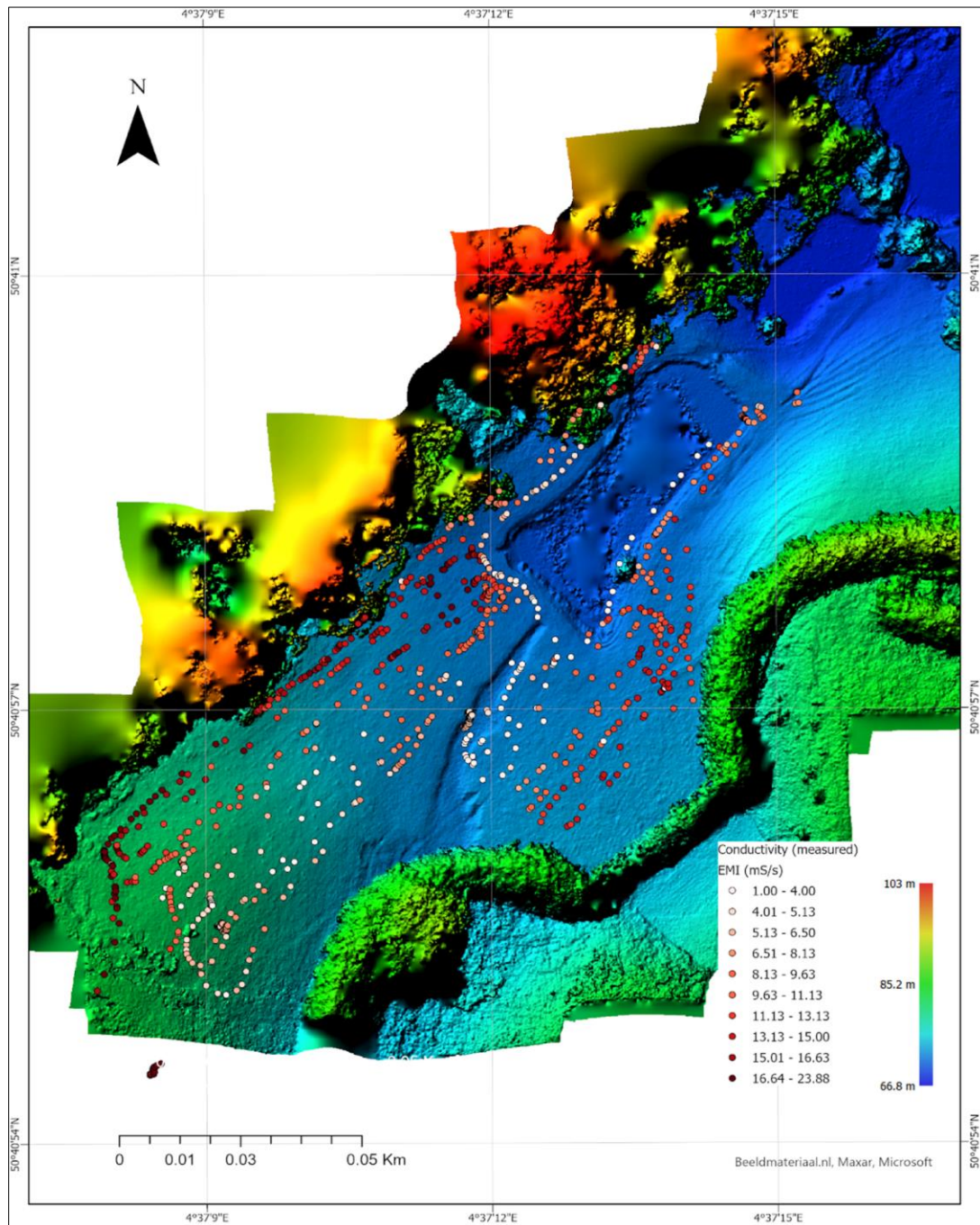


Figure 20: Comparison between EMI and DSM results

The canopy height model in the DSM above showed that the areas where the highest conductivity was measured along the sides of the field had high crown cover. The areas with high vegetation

cover as canopies, serve as a soil cover to help the soil retain its moisture content. In these areas, we observed high conductivity at the boundaries of the field, where we recorded high vegetation showing high moisture content in the soil.

Because vegetation cover affects water retention in the soil, it is a possible explanation for the observed high EC in these areas. Besides retaining more moisture, the presence of vegetation in these areas also affects soil salinity and infiltration by enhancing capillary activities in the soil, which can influence the soil EC.

5. Conclusion

The results of the analyses conducted in this research complement each other. They are an indication that the application of these technologies can be used to study the surface and subsurface properties of the soil. GRP and EMI were used to understand the soil properties with regard to its moisture content, salinity, and other particles in the subsurface. On the other hand, photogrammetry through the generation of the DSM reflects the crown heights at specific parts of the study area. The results from photogrammetry gave a possible explanation for the results obtained using EMI and GPR.

The methodologies applied in this study were non-invasive to the environment. One key point to note from the participants was the importance of data collection strategies, particularly as it affects the results and interpretation of the modelled soil condition. Despite the few lapses in the data collected, as explained earlier, it was possible to understand the characteristics of the study area as it relates to the properties of the soil, subsoil and surface vegetation cover.

6. Bibliographic references

- Gish, T. J., Dulaney, W. P., Kung, K. S., Daughtry, C. S., Doolittle, J. A., & Miller, P. T. (2002). Evaluating use of ground-penetrating radar for identifying subsurface flow pathways. *Soil Science Society of America Journal*, 66(5), 1620-1629. doi:10.2136/sssaj2002.1620
- Hapke, C., & Richmond, B. (2000). Monitoring Beach morphology changes using small-format aerial photography and digital softcopy photogrammetry. *Environmental Geosciences*, 7(1), 32-37. doi:10.1046/j.1526-0984.2000.71001.x
- Huang, J., Taghizadeh-Mehrjardi, R., Minasny, B., & Triantafilis, J. (2015). Modeling soil salinity along a hillslope in Iran by inversion of EM38 Data. *Soil Science Society of America Journal*, 79(4), 1142-1153. doi:10.2136/sssaj2014.11.0447
- Ivan Jakopec, Ante Marendić, & Igor Grgac. (2022). A Novel Approach to Landslide Monitoring based on Unmanned Aerial System Photogrammetry. *Rudarsko-geološko-Naftni Zbornik*, 37(5), 83–101. <https://doi.org/10.17794/rgn.2022.5.8>
- Li, X., Zhang, Y., Jin, X., He, Q., & Zhang, X. (2017). Comparison of digital elevation models and relevant derived attributes. *Journal of Applied Remote Sensing*, 11(4), 046027.
- Lombardi, F., Podd, F., & Solla, M. (2022). From its core to the niche: Insights from GPR Applications. *Remote Sensing*, 14(13), 3033. doi:10.3390/rs14133033
- Martinez, G., Huang, J., Vanderlinden, K., Giráldez, J. V., & Triantafilis, J. (2018). Potential to predict depth-specific soil-water content beneath an olive tree using electromagnetic conductivity imaging. *Soil Use and Management*, 34(2), 236-248. doi:10.1111/sum.12411
- Marzolf, I., & Poesen, J. (2009). The potential of 3D gully monitoring with GIS using high-resolution aerial photography and a digital photogrammetry system. *Geomorphology*, 111(1-2), 48-60. doi:10.1016/j.geomorph.2008.05.047
- Moghadas, D., Jadoon, K. Z., & McCabe, M. F. (2017). Spatiotemporal monitoring of soil water content profiles in an irrigated field using probabilistic inversion of time-lapse EMI data. *Advances in Water Resources*, 110, 238-248. doi:10.1016/j.advwatres.2017.10.019
- Othoman Che, N. N., Mohd, N. md I., Ismail, R. C., Muhammad, I. A., & Hui, C. K. (2020). Factors that affect soil electrical conductivity (EC) based system for smart farming application. *The 2nd international conference on applied photonics and electronics 2019 (inCape 2019)* <http://dx.doi.org/10.1063/1.5142147>
- Saey, T., Delefortrie, S., Verdonck, L., De Smedt, P., & Van Meirvenne, M. (2014). Integrating EMI and GPR data to enhance the three-dimensional reconstruction of a circular ditch system. *Journal of Applied Geophysics*, 101, 42-50. doi:10.1016/j.jappgeo.2013.11.004

T. Saarenketo, Electrical properties of road materials and subgrade soils and the use of ground penetrating radar in traffic infrastructure surveys, Ph.D. thesis, University of Oulu, Oulu, Finland, 2006

Teoh, Y., Bruka, M., Idris, N., Ismail, N., & Muztaza, N. (2018). Introduction of a ground penetrating radar system for subsurface investigation in Balik Pulau, Penang Island. *Journal of Physics: Conference Series*, 995, 012098. doi:10.1088/1742-6596/995/1/012098

Walstra, J., Chandler, J. H., Dixon, N., & Dijkstra, T. A. (2007). Aerial Photography and digital photogrammetry for landslide monitoring. *Geological Society, London, Special Publications*, 283(1), 53-63. doi:10.1144/sp283.5

Yan, Y., Yan, Y., Zhao, G., Zhou, Y., & Wang, Z. (2022). Combined ERT and GPR data for subsurface characterization of weathered hilly slope: A case study in Zhejiang Province, Southeast China. *Sustainability*, 14(13), 7616. doi:10.3390/su14137616

7. Annexes

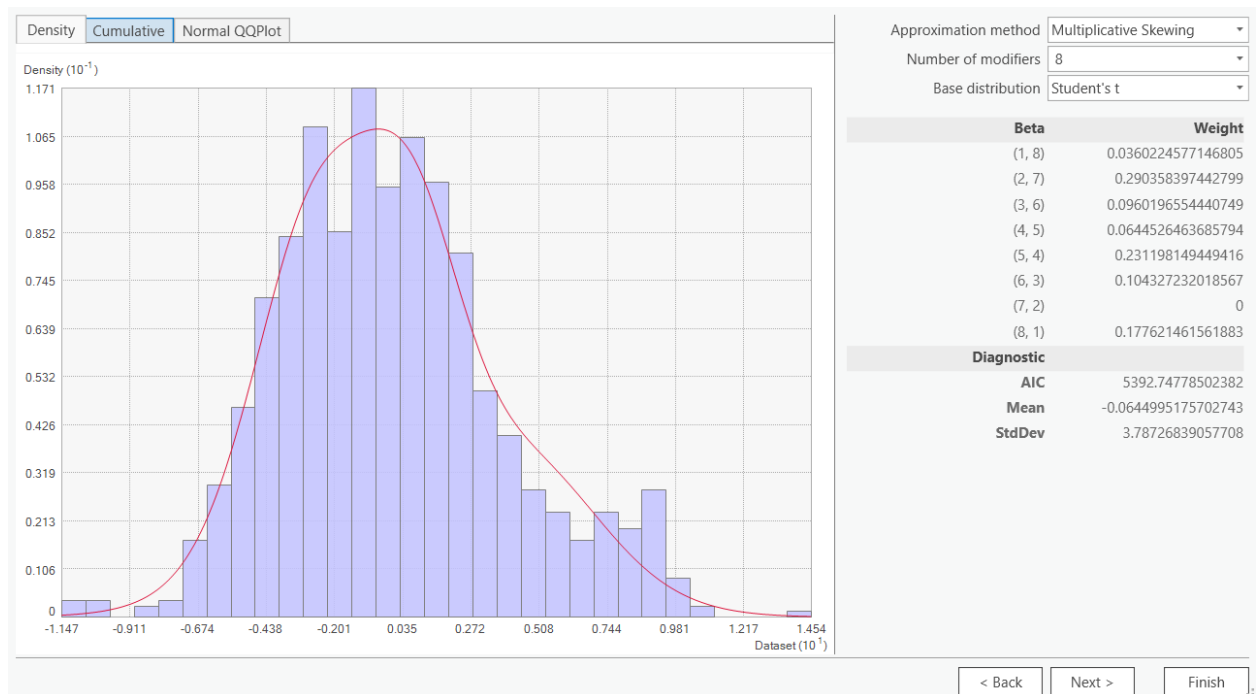


Figure A1: Normal distribution curve of the data

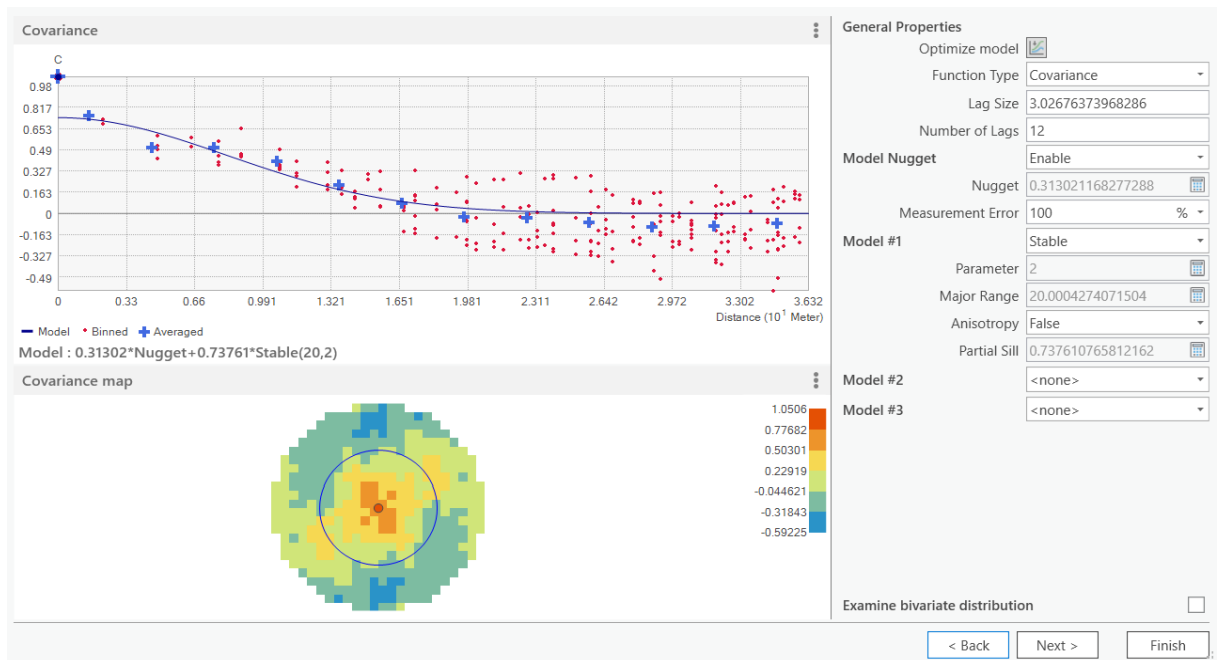


Figure A2: semi-variogram

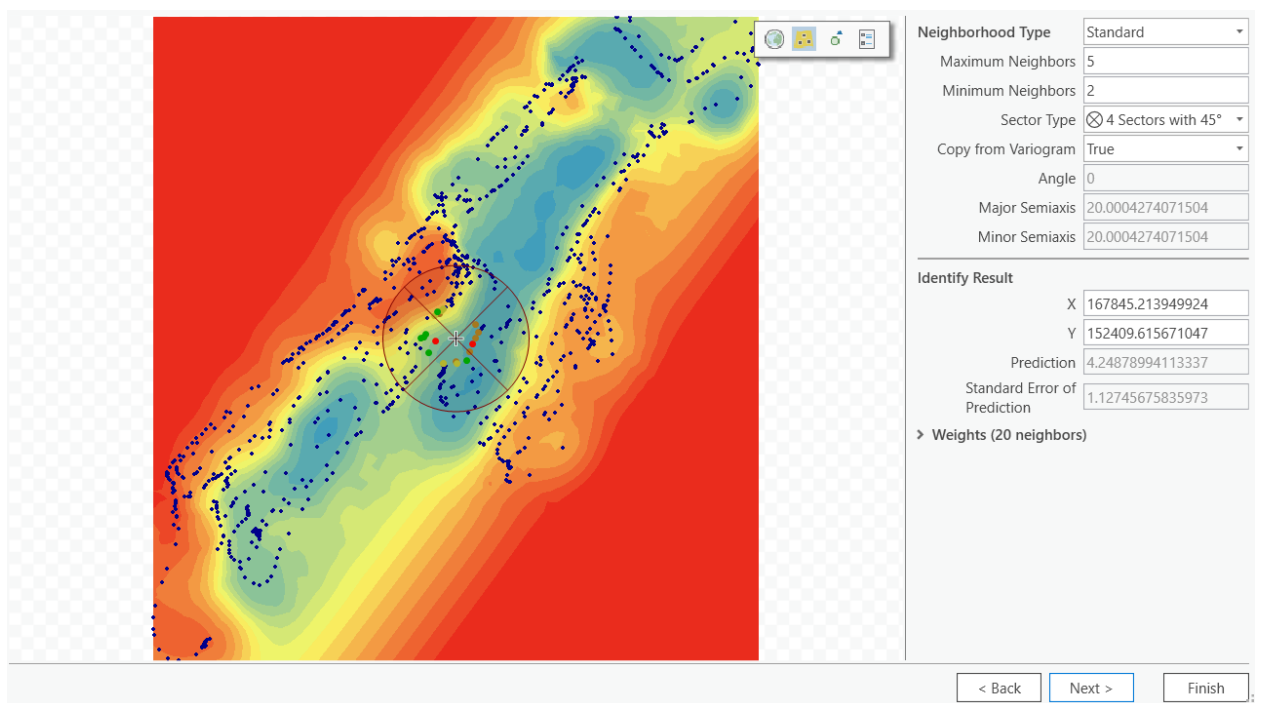


Figure A3: Searching neighbor analysis

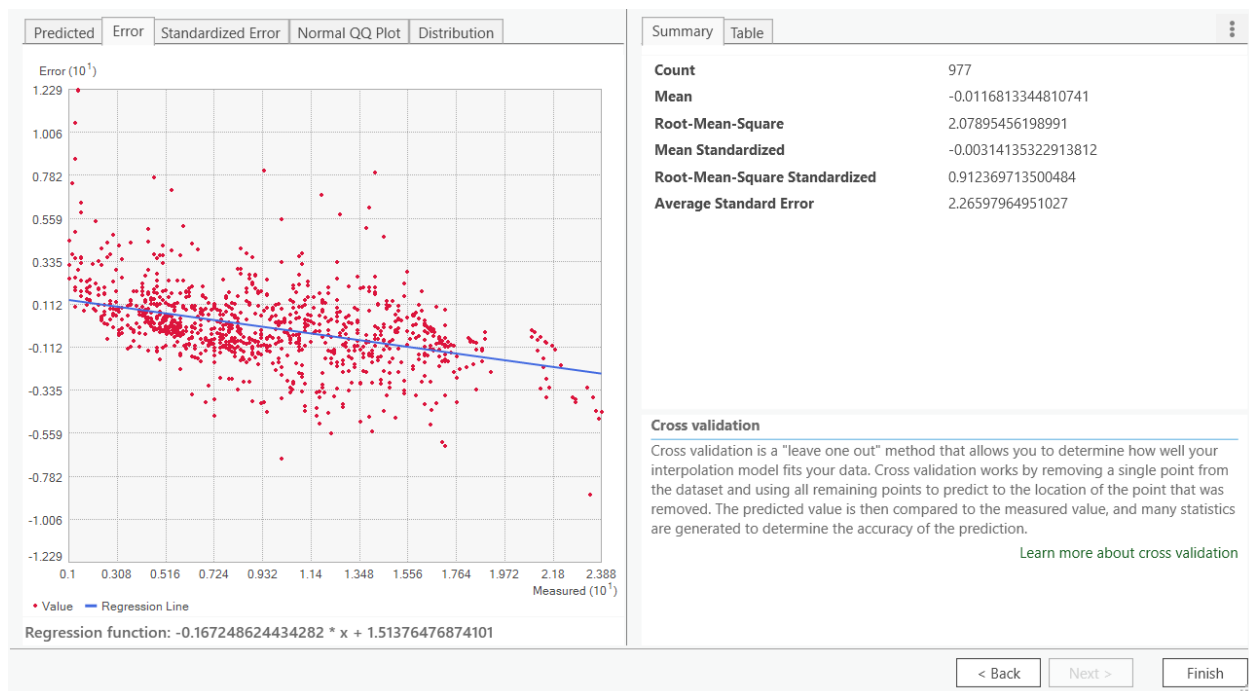
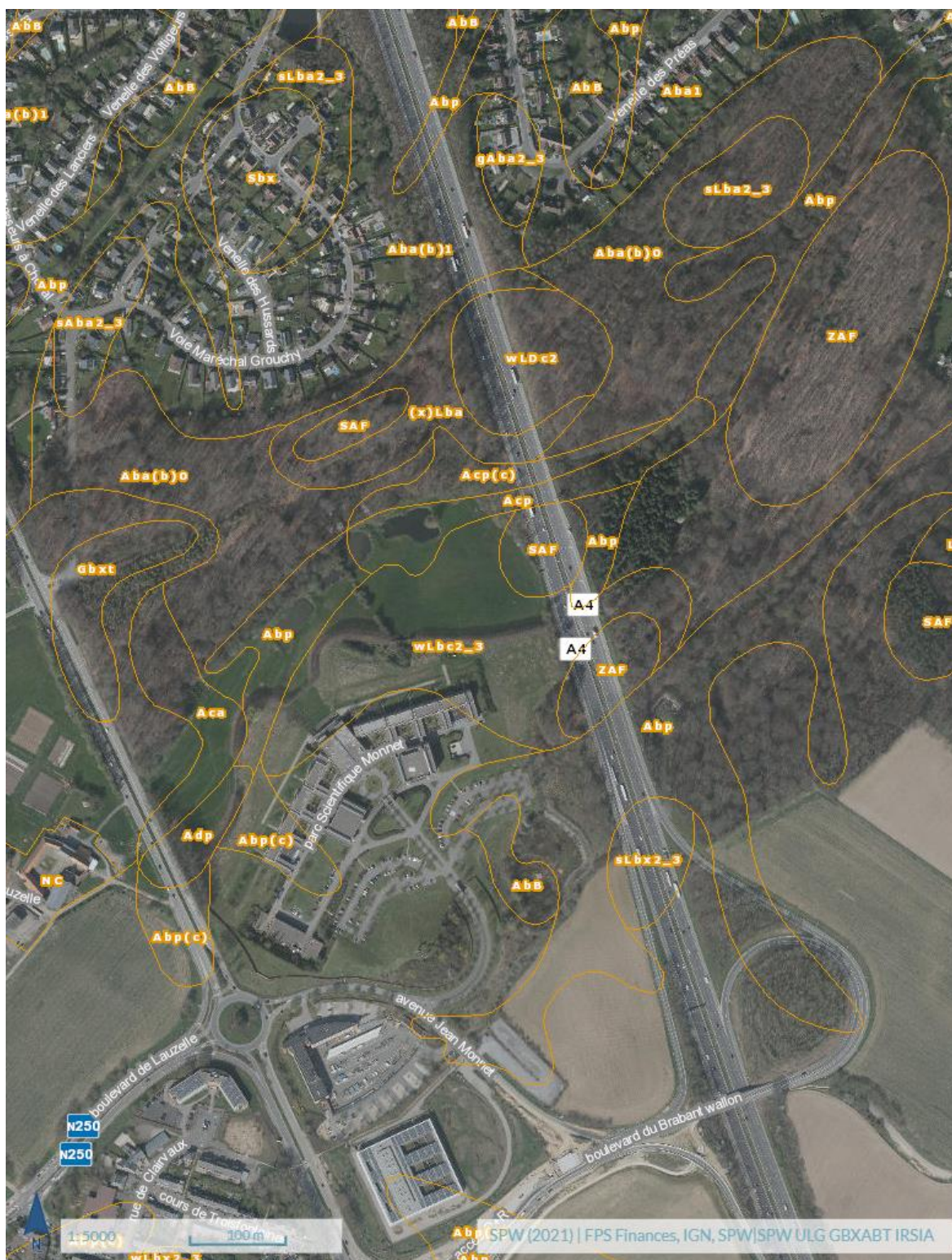
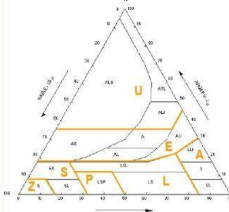


Figure A4: Cross-validation of the model



Legend: [https://www.fichierecologique.be/resources/LCNSW TableauSimplifie.pdf](https://www.fichierecologique.be/resources/LCNSW_TableauSimplifie.pdf)

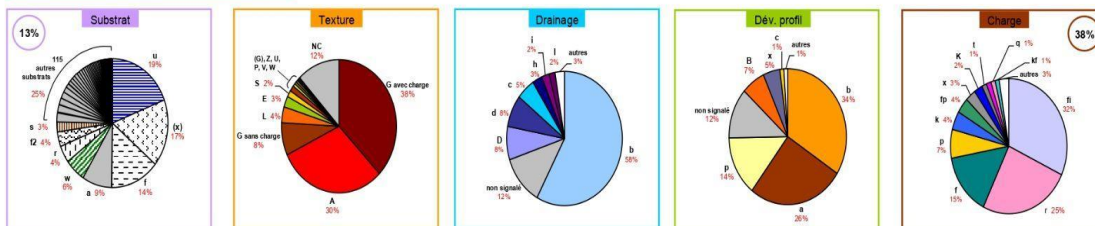
LÉGENDE DE LA CARTE NUMÉRIQUE DES SOLS DE WALLONIE - TABLEAU SIMPLIFIÉ*

SÉRIES DÉRIVÉES	TEXTURE	SÉRIES PRINCIPALES	DÉVELOPPEMENT DE PROFIL	CHARGE EN ÉLÉMENTS GROSSIERS
SUBSTRAT <i>Préfixe de la série principale</i> a fortement altéré f schisteux g caillouteux / graveleux j de grès calcaire k calcaire m de macigno n crayeux / crayeux ou mameux p psammitique q gréseux r schisto-gréseux s sableux u argileux v tourbeux w argilo-sableux x non défini / de silexite .u d'argile d'altération de .w de sable argileux d'altération de (.) Substrat débutant entre 80 et 125 cm de profondeur pour les sols non caillouteux (< 5%) .. Profondeur variable d'appartenance du substrat .f Substrat discontinu spatialement si G... Substrat indiqué si "aberrant" (nature lithologique différente de la charge) Si substrat "normal" : à déduire de la charge et du fait d'une phase de profondeur	1^{ère} position de la série principale (X...) Sols organiques V Tourbe (> 30% M.O.) W Tourbière haute intacte (inactive) Sols minéraux Z Sable S Sable limoneux P Limon sableux léger L Limon sableux A Limon E Argile légère U Argile lourde (G) Limon peu caillouteux (sols p ¹) G Limon peu caillouteux (sols non p) L Limon caillouteux (sols p) L Limon (très) caillouteux (sols non p) COMPLEXES  1 sols sans développement de profil 2 dans la plupart des cas	2^{ème} position de la série principale (...XX) Textures L, A, E, U, G - Textures Z, S, P Drainage : Définition - sols : a excessif très secs - - b favorable non gleyifiés > 125 - c modéré faiblement gleyifiés 80-125 - d imparfait modérément gleyifiés 60-90 - d imparfait modérément humides 50-80 - d imparfait modérément humides 40-60 - à engorgement d'eau temporaire - sans horizon réduit h assez pauvre fortement gleyifiés 30-50 - h assez pauvre humides 20-40 - i pauvre très fortement gleyifiés 0-30 - i pauvre très humides 0-20 - à engorgement d'eau permanent - à horizon réduit e assez pauvre fortement gleyifiés 30-50 > 80 e assez pauvre humides 20-40 > 80 f pauvre très fortement gleyifiés 0-30 40-80 f pauvre très humides 0-20 40-80 g très pauvre réduits < 40 g très pauvre extrêmement humides < 40 COMPLEXES A (a)+b+c+d I h+I B a+b F e+f D c+d G e+fg	3^{ème} position de la série principale (...XX) Horizon : a B textural b B structural c B textural fortement tacheté (textures A, L) ou morcelé (textures Z, S, P) d B textural jaune rougeâtre f B humique ou/et ferrugine peu distinct g B humique ou/et ferrugine distinct h B humique ou/et ferrugine morcelé m A humifère anthropogène épais p Absence de développement de profil x Développement de profil non défini COMPLEXES B a+b F fg(+b) P p+b / p+x	4^{ème} position de la série principale (...XX) f schisteuse fi schisto-psammitique fp schisto-gréseuse fq calcaire k argilo-calcaire kf schisto-calcaire m de macigno n crayeuse p psammitique q gréseuse r schisto-gréseuse t de gravier x de silexite 1 pour les sols G non p (très) caillouteux pour les sols Z, S, P et U à plus de 5%
SÉRIES SPÉCIALES Sols artificiels OE Fosse d'extraction ON Remblai OT Terrain remanié Terrains non différenciés B Zone de source H Complexe de sols sur fortes pentes J Affleurement rocheux R Ravin ou fond de vallon rocaillieux S Fond de vallon limoneux NON CARTOGRAPHIÉ NC Zones non cartographiées (zones, bûches, cours d'eau, canaux, marais, routes, chemins de fer, domaines militaires, ...)	VARIANTES DE MAT. PARENTALE MEUBLE <i>Suffixe de la série principale</i> a Sols sur limon d'altération (G...a) y Sols devenant plus fins (Z, S) ou plus lourds (L, A, E) en profondeur z Sols devenant plus grossiers (Z, S) ou plus légers (L, A, E) en profondeur	PHASES DIVERSES <i>Suffixe de la série principale</i> Phases liées à la charge en éléments grossiers en surface PHASE : (q) à (gros) cailloux (ou blocs) gréseux (ou quartzitiques) épars (en surface) (r) à charge modérée de petits cailloux non phyllitiques 1 peu caillouteuse c caillouteuse Phases liées à l'altération (a) Phase à débris de roches fortement altérées b Phase rougeâtre Phase liée à la matière organique (v) Phase à couverture tourbeuse	VARIANTES DE DÉV. DE PROFIL <i>Suffixe de la série principale</i> Sols des plateaux et des pentes : A (L/P/S) - a (b/c/x) (b) Horizon B textural tacheté 0 Horizon A ¹ : épais (> 40 cm) 1 Horizon A ¹ : mince (< 40 cm) A b(c/d) B Développement : 1 profond (> 125 cm) 2 moyennement ou peu profond (40-125 cm) 3 superficiel (< 40 cm) Sols des vallées et des dépressions (..p) : (c) Horizon B : entre 40 et 80 cm 1 textural enfoui : entre 80 et 125 cm 0 Colluvions ou alluvions de plus de 125 cm 1 ancienne nomenclature (A1+A2) → A+E Phase liée au relief P Complexe des pentes fortes Phase anthropique /o Phase à (forte) influence anthropique	PHASES DE PROFONDEUR <i>Suffixe de la série principale</i> Sols non caillouteux (< 5%) et sols organiques SUBSTRAT DÉBUTANT (1) entre 80 et 125 cm 2 entre 40 et 80 cm 3 entre 20 et 40 cm Sols : 0 à plus de 125 cm : x x x 1 entre 80 et 125 cm : x x x 2 entre 40 et 80 cm : x x x 3 entre 20 et 80 cm : x x x 7 entre 40 et 80 cm : x x x 4 entre 20 et 40 cm : x x x 5 entre 20 et 40 cm : x x x 6 à moins de 20 cm : x x x 1 nature du substrat en préfixe entre parenthèses

* Les sigles dont les symboles sont repris dans ce tableau simplifié couvrent 97% du territoire de la Région wallonne.

Figure A6: Soil map legend 1

Ventilation des sols de la CNSW par type de symboles



S. DÉRIVÉES					SÉRIES PRINCIPALES				VARIANTES		PHASES		SÉRIES SPÉCIALES	30 sigles (sur un total de 6295) couvrent 50% du territoire de la Région wallonne... (466 sigles couvrent 90%)			
Substrat	Texture	Drainage	Dév. profil	Charge	de dev. de prof.	de prof. diverses	ha	% RW	% cum	Définition							
NC													OT	138632	8,2	8,2	Non cartographié
Aba1	A	b	a			1								96235	5,7	13,9	Sol limoneux à horizon B textural, phase à horizon A mince
Gbbf2	G	b	b	fi		2								88228	5,2	19,1	Sol limono-caillouteux à charge phylladeuse, à horizon B structural, phase peu profonde
Gbbf0_1	G	b	b	fi		0_1								57737	3,4	22,5	Sol limono-caillouteux à charge phylladeuse, à horizon B structural, phase profonde ou moyennement profonde
Gbb2	G	b	b	r		2								45542	2,7	25,2	Sol limono-caillouteux à charge schisto-gréseuse, à horizon B structural, phase peu profonde
Gbb0_1	G	b	b			0_1								36299	2,1	27,4	Sol limoneux peu caillouteux, à horizon B structural, phase profonde ou moyennement profonde
Aba(b)1	A	b	a		(b)	1								33439	2,0	29,4	Sol limoneux à horizon B textural tacheté, phase à horizon A mince
Gbbf2	G	b	b	f		2								32077	1,9	31,2	Sol limono-caillouteux à charge schisteuse, à horizon B structural, phase peu profonde
Gbbf4	G	b	b	f		4								24012	1,4	32,7	Sol limono-caillouteux à charge schisteuse, à horizon B structural, phase superficielle
Abp(c)	A	b	p		(c)									23284	1,4	34,0	Sol sur limon à horizon B textural enfoui à faible profondeur
Ada1	A	d	a			1							21766	1,3	35,3	Sol limoneux modérément gleyifié, à horizon B textural, phase à horizon A mince	
Aca1	A	c	a			1							20845	1,2	36,6	Sol limoneux faiblement gleyifié, à horizon B textural, phase à horizon A mince	
Aba(b)0	A	b	a		(b)	0							19427	1,1	37,7	Sol limoneux à horizon B textural tacheté, phase à horizon A épais	
OT													16940	1,0	38,7	Terrain remanié	
Ada0	A	d	a			0							15856	0,9	39,7	Sol limoneux modérément gleyifié, à horizon B textural, phase à horizon A épais	
Abp	A	b	p										15843	0,9	40,6	Sol sur limon	
Gbbf0_1	G	b	b	r		0_1							15447	0,9	41,5	Sol limono-caillouteux à charge schisto-gréseuse, à horizon B structural, phase profonde ou moyennement profonde	
AbB	A	b	B										14947	0,9	42,4	Sol limoneux à horizon B textural ou à horizon B structural	
ADp	A	D	p										14474	0,9	43,2	Sol faiblement ou modérément gleyifié sur limon	
Gbbk4	G	b	b	k		4							13925	0,8	44,1	Sol limono-caillouteux à charge calcaire, à horizon B structural, phase superficielle	
Gbbp2	G	b	a	p		2							12771	0,8	44,8	Sol limono-caillouteux à charge psammitique, à horizon B textural, phase peu profonde	
(x)Aba	A	b	a										12004	0,7	45,5	Sol limoneux à horizon B textural, substrat débutant à profondeur moyenne	
ADa1	A	D	a			1							11888	0,7	46,2	Sol limoneux faiblement ou modérément gleyifié, à horizon B textural, phase à horizon A mince	
Aba0	A	b	a			0							11678	0,7	46,9	Sol limoneux à horizon B textural, phase à horizon A épais	
ADa0	A	D	a			0							10399	0,6	47,5	Sol limoneux faiblement ou modérément gleyifié, à horizon B textural, phase à horizon A épais	
OE													10259	0,6	48,2	Fosse d'extraction	
Gbbf2(r)	G	b	b	fi		2				(r)			9902	0,6	48,7	Sol limono-caillouteux à charge phylladeuse, à horizon B structural, phase peu profonde, à charge modérée de petits cailloux non phyllitiques	
Gbbp4	G	b	a	p		4							9658	0,6	49,3	Sol limono-caillouteux à charge psammitique, à horizon B textural, phase superficielle	
Abp0_1	A	b	p		0_1								9303	0,6	49,9	Sol sur limon profond ou à horizon B textural enfoui à profondeur moyenne	
fGbb2	f	G	b	b		2							9289	0,5	50,4	Sol limoneux peu caillouteux, à horizon B structural, phase peu profonde à substrat schisteux	

Figure A7: Soil map legend 2

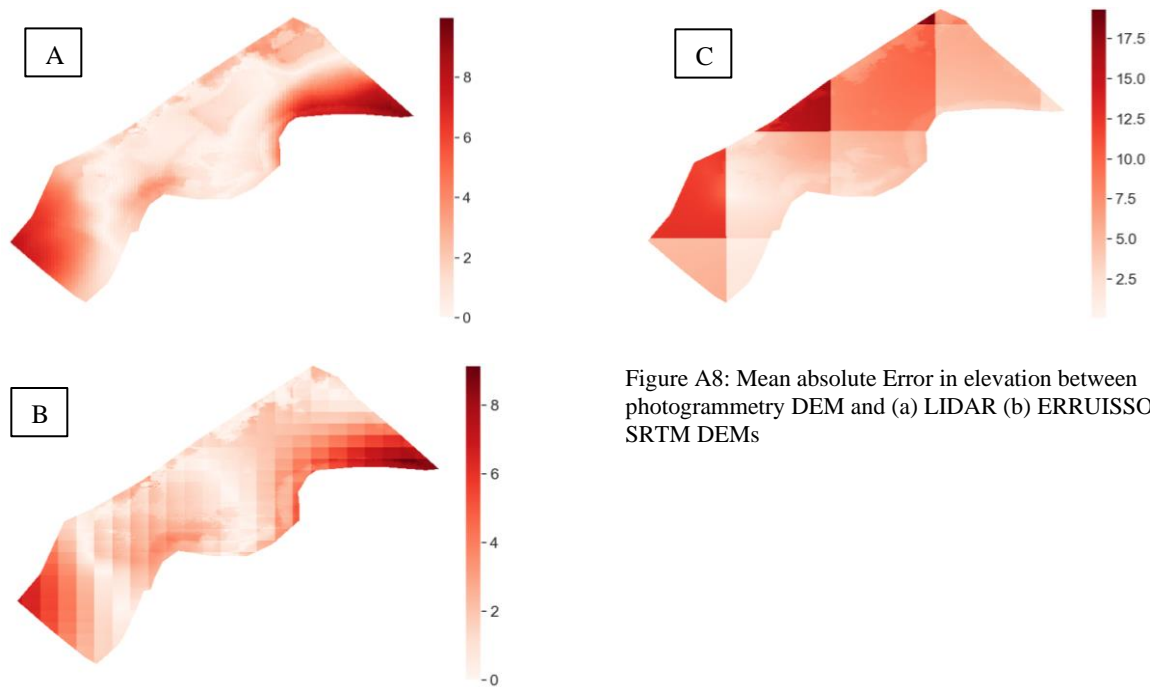


Figure A8: Mean absolute Error in elevation between photogrammetry DEM and (a) LIDAR (b) ERRUISSOL (c) SRTM DEMs